Measurement of the 2D emission profiles of hydrogen and impurity ions in the TCV divertor

A. Perek [a],*, B.L. Linehan [b], M. Wensing [c], K. Verhaegh [d], I.G.J. Classen [a], B.P. Duval [c], O. Février [c], H. Reimerdes [c], C. Theiler [c], T.A. Wijkamp [a], M.R. de Baar [a], the EUROfusion MST1 team[1], the TCV team[2]

[a] *Dutch Institute for Fundamental Energy Research, De Zaale 20, 5612 AJ Eindhoven, Netherlands*
[b] *Plasma Science and Fusion Center, Massachusetts Institute of Technology, 77 Massachusetts Avenue, NW17 Cambridge, MA 02139, USA*
[c] *Ecole Polytechnique Fédérale de Lausanne (EPFL), Swiss Plasma Center (SPC), CH-1015 Lausanne, Switzerland*
[d] *CCFE, Culham Science Centre, Abingdon, Oxon OX14 3DB, United Kingdom*

ARTICLE INFO

Keywords:
Quantitative imaging
Tomographic inversion
Detachment
2D spectroscopy

ABSTRACT

Plasma emission of hydrogen and impurities is measured with use of filtered camera imaging in TCV divertor. The measurement technique is discussed in detail including: selection choice of filters, the absolute calibration procedure and the tomographic inversion. The process is applied to an unseeded L-mode density ramp discharge in an unfavorable for H-mode access magnetic field direction with divertor baffles. Obtained poloidal emission profiles are used to split Balmer emission into excitation and recombination parts revealing a recombination emission maximum on the high field side. The optical emission is further studied by selecting radial profiles in cross sections of interest finding an opposite radial shift direction for high and low n Balmer line emission maxima in detached conditions.

1. Introduction

Safe power exhaust is one of the key challenges to realize nuclear fusion on a power plant scale. In a large fusion device, such as DEMO, a significant fraction of power will be exhausted in form of the core radiation. However, not all fusion power can be radiated in the core, to achieve and maintain improved confinement modes, a fraction of the power must constantly cross the last closed flux surface. Outside the confined region, the power enters the Scrape-Off Layer (SOL), where it is diverted towards relatively small target surfaces. This results in relatively high heat and particle fluxes to the target; if unmitigated, those fluxes can erode and melt those surfaces. To avoid damage, the power exhaust can be operated in a so called detached regime [1] where low-Z impurities are actively seeded to radiate at the plasma edge and maximize the spread of the power through line radiation. Then, a portion of the remaining power is spent on interaction with the background gas through excitation, ionization, charge exchange and a range of molecular reactions before being deposited at the target.

At TCV, the detachment processes were studied using line of sight integrated spectroscopy [2], filtered camera imaging [3–6], thermography [7,8], wall and reciprocating probes [9,10]. The experimental data can provide input for comparisons with flux-resolved plasma models aiming to capture the balance between plasma processes and changes between experiments [11]. As the plasma models gained fidelity, the comparisons with the experiments yielded good agreements uncovering the mechanisms behind target profile asymmetry [12], geometry related detachment threshold observations [13] and recently taking the lead in predicting the X-point potential well [14].

The advancement in modeling left the flux-resolved spectroscopic measurement techniques lagging behind, leaving the radial emission profiles as unresolved for over two decades [15,2,16]. Those profiles hold the key to detailed comparisons between experiment and modeling. In the past, many camera systems were developed to study the emission profiles [17–21]. At TCV, a significant effort was made towards the measurement of those profiles with the MultiCam [22,23], the Multi-Spectral Imaging diagnostic [24] and now with the Multispectral

Advanced Narrowband Tokamak Imaging System (MANTIS) [25].

In this paper, we present the measurement of the 2D emission profiles for hydrogen and impurities together with its uncertainty quantification. The paper is structured as follows, the MANTIS system is described together with a selection of interference filters, their limitations and the absolute calibration technique. Then the tomographic inversion process is presented together with its uncertainty propagation through a Monte Carlo method. Resulting emissivity is analyzed with an adaptation of an existing spectroscopic technique [2] to split the emission between excitation and recombination parts. The emission features are studied and an explanation is proposed.

2. Intensity measurement with filtered cameras

To infer flux-resolved dominance of different plasma processes in the divertor, one requires a diagnostic capable of resolving absolute intensity of multiple emission lines in the poloidal plane. In this work we employ the MANTIS system to image the emission [25,26]. MANTIS is a cavity-based imaging polychromator designed to resolve 2D absolute intensity images of 10 different emission lines with the same view and spatial resolution $< 5\,\mathrm{mm}$. Such imaging systems provide integrated intensity of emission under the filter raising the question of what portion of the signal comes from the emission line of interest.

To answer this question, one needs to understand the limitations of the system. In MANTIS's cavity [27], the light passes interference filters with an angular distribution ranging from 0.7 to 5.5 deg, as a result, the light rays experience the filter's transmission curve shifted [28]. The shift can be calculated according to the equation below:

$$\frac{\lambda}{\lambda_0} = \sqrt{1 - \frac{\sin^2\theta}{n_{eff}^2}}. \tag{1}$$

The relative shift depends on the angle of incidence θ which depends on the location in the image and the effective refractive index n_{eff}. This results in a minimum bandwidth of approximately $1.2 - 1.8\,\mathrm{nm}$ for which the transmission has negligible dependence on the angle at the wavelength of interest. This lower limit implies that not all emission lines can be separated from their surrounding in MANTIS. It is particularly problematic for weak emission lines with relatively strong neighboring impurity lines. Among filters used in this work, $D_{7\rightarrow2}$ can have significant contributions from $O\,II, O\,III$ and $He\,I$ lines. This pollution depends strongly on the experimental conditions. Fig. 1a) shows spectrally resolved measurements of $D_{7\rightarrow2}$ using the Divertor Spectroscopy System

(DSS) [2] together with the filter curve measured with collimated light and shifted to $\theta = 3\,\mathrm{deg}$ using $n_{eff} = 1.8$. The locations of the edge DSS chords are presented in Fig. 7. The figure shows spectra from chord 15 which is roughly the middle of the outer divertor leg at two line averaged densities $< n_e >= [1 \cdot 10^{20}, 1.3 \cdot 10^{20}]\,\mathrm{m}^{-3}$ representing attached and detached divertor conditions respectively. As the density increases, the $D_{7\rightarrow2}$ brightness increases while the neighboring impurity lines decrease.

Those impurity contributions were quantified by multiplying the spectrum with the filter's curve and integrating the emission for the filter's transmission thresholded at 0.001. Then, the $D_{7\rightarrow2}$ emission was separately integrated and the fraction of signal $f_{D_{7\rightarrow2}}^{signal}$ due to $D_{7\rightarrow2}$ emission was computed. The result is presented in Fig. 1b). As the density increases the $f_{D_{7\rightarrow2}}^{signal}$ reaches approximately 1 showing that the $D_{7\rightarrow2}$ can be quantitatively measured in MANTIS, depending on the experimental conditions. The same study was conducted for $D_{3\rightarrow2}, D_{4\rightarrow2}, D_{5\rightarrow2}$ yielding $f^{signal} \approx 1$ regardless of plasma conditions. The $D_{6\rightarrow2}$ and $D_{8\rightarrow2}$ were found unsuitable due to their relatively nitrogen and oxygen pollution respectively. Thus, strongly limiting the use of MANTIS for measurements of the high-n Balmer series with $D_{9\rightarrow2}$ as a potential candidate. However, the brightness of $D_{9\rightarrow2}$ could limit the measurement capability.

In MANTIS, two different locations on the image can have a different effective angle θ_{eff} defined as the angle matching the shift of the transmission curve with respect to normal light incidence. This can result in a wavelength dependent vignetting at the filter for optical designs with a wide angular range, we will refer to it as *spectral vignetting*. To account for it in the calibration, one needs two measure the vignetting profile with two separate light sources: an incandescent light source and a spectral lamp, both sources are then coupled to the system through integrating spheres. The first source provides the absolute calibration image together with system's broadband vignetting profile. Then, the spectral source provides the measurement of the total vignetting profile consisting of both broadband and spectral components at the wavelength of the source. Provided that the peak transmission of the filter falls within the image, the spectral vignetting profile can be normalized to the peak transmission yielding pixel per pixel transmission measurement of the filter at the wavelength of the source. Those two measurements combined provide the absolute intensity calibration. Breakdown of the uncertainty estimate for the calibration procedure is presented in Table 1.

3. Tomographic inversions

To obtain quantitative information about plasma emissivity, the images must be tomographically inverted. This process can create unphysical artifacts and misplace the emission affecting further analysis. In this section, we present our inversion process together with the uncertainty propagation and determine the role of inversion artifacts in the process.

Before obtaining inversions, one should determine what are the plasma features present in the input image. For this purpose, a representative image was selected. A good example is $D_{5\rightarrow2}$ emission during the outer target ion saturation current rollover in an L-mode discharge with the ∇B drift away from the X-point i.e. magnetic field direction
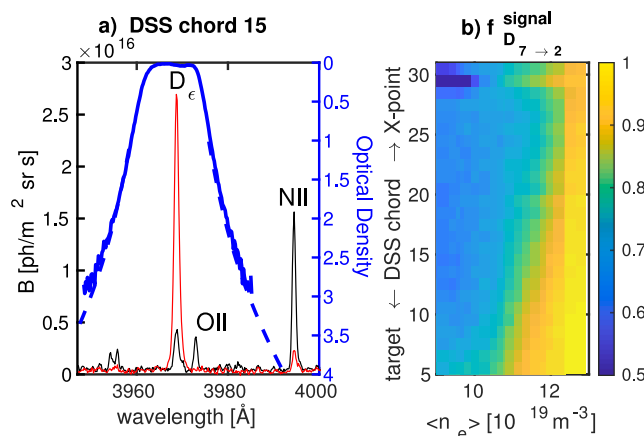

Fig. 1. Measurement of the signal pollution in MANTIS using line integrated spectroscopy on the outer target with the DSS for two line averaged densities: black at $1 \cdot 10^{20}\,\mathrm{m}^{-3}$; red at $1.3 \cdot 10^{20}\,\mathrm{m}^{-3}$. The filter curves are shown in blue while the chords are numbered from the closest to the target to the closest to the X-point. TCV #63974. (For interpretation of the references to colour in this figure legend, the reader is referred to the web version of this article.)

Table 1
Absolute intensity calibration uncertainty estimation.

Source	Estimate [%]
Stray light in the cavity	< 2
Spectral vignetting measurement	< 5
Broadband source calibration	< 10
Calibration reproducibility	< 3
Total	< 12

unfavourable for H-mode access.

Fig. 2 presents such a frame with the following identified features: outer target common flux (1), private flux (2), the gap between common and private flux (between 1 and 2), outer and inner targets (3,4), the overlap between the outer target and the private flux (5), inner and outer baffle interaction (6,7), emission near the X-point (8) and the upstream emission for inner and outer targets and far SOL (9,10).

The first step to obtain an inversion is to infer the camera pupil location and its distortion coefficients. This was achieved by point fitting locations in the image to a CAD model of TCV using Calcam [29]. The output is then used to cast rays from the pupil to the walls of the model for each pixel in the image [29]. Those rays are then used to generate a geometry matrix (GM) that relates emissivities in the inversion grid with the pixel values in the image [29]. This yields a relation between the pixel values in the image *img* and the inverted emissivity *inv* as:

$$img = GM \cdot inv \qquad (2)$$

To solve the equation above for the emissivity, the Simultaneous Algebraic Reconstruction Technique (SART) [30] was used assuming toroidal symmetry.

This technique is an active area of research with efforts towards accounting for reflections in the metallic-wall machines [29–32,21,19]. In case of TCV, its carbon tiles mainly absorb light with diffusive instead of specular reflections. The surplus or deficit of light in the reconstructed emissivity can be determined by forward-modeling the inversion and computing the relative difference with respect to the input image. *In this work, this approach was adopted to iteratively add or subtract light from the input image with the aim of obtaining an inversion that matches the original input image when forward-modeled.* The approach can be formalized as:

$$img_{m+1} = img_m (1 + (img_0 - FM_m)/img_0) \qquad (3)$$

where $FM_m = GM \cdot inv_m$ is the forward modeled image of the inversion m while img_0 is the original image acquired in the tokamak.

The progress of this algorithm is presented in Fig. 3 for iterations $m =$
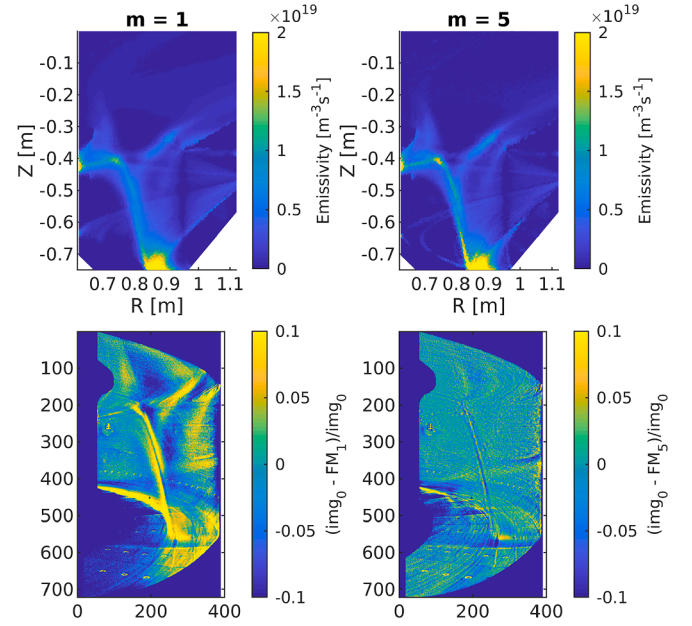
Fig. 3. Progress of the iterative inversion process for $D_{5\to2}$. Top row: emissivities for selected iterations. Bottom row: relative error of forward modeled image with respect to the input image. TCV # 63974, $t = 1.315$ s.

[1, 5] together with their relative difference to the original image. The figure shows over 10% deviation for the first iteration over both private and common flux. As the algorithm iterates, the relative differences converge towards zero with exception of the non-toroidally symmetric features such as screw heads or tile edges. Those features cannot be reproduced under the assumption of toroidal symmetry, their positive feedback will amplify them decreasing the convergence. The center column was found to be a good example of that due to its proportion of toroidally symmetric and asymmetric features. To resolve this issue, the rays terminating at the center column were removed from the process. In this method, it is difficult to define the termination criterion as the non-toroidally symmetric features dominate the relative error after few iterations. To avoid this, the process is terminated after 2 to 5 iterations depending on the case.

Apart from producing all of the features in the sample image, the algorithm creates a horizontal V-shaped artifact originating from the location of the camera. The inversion artifact becomes slightly less pronounced for later iterations. However, it remains in the inversion as if it was an essential or unrelated feature in matching the input image. The role of the artifact becomes more apparent in the following noise propagation analysis.

The SART algorithm iteratively minimizes the norm between the input image and its forward modeled inversion, as a result, there is no exact transfer function to quantify the uncertainty of each inversion cell. Therefore, we resort to numerical methods of uncertainty propagation by applying the Monte-Carlo approach by feeding perturbed images to obtain their respectively perturbed inversions. To generate those sample images, the signal to noise ratio (SNR) of each pixel in the image was used to generate perturbations with normal distribution. Those images were then inverted and the standard deviation of each cell was computed.

Resulting distribution of SNR as a function of emissivity is presented in Fig. 4a), while its spatial distribution is shown in Fig. 4b). The spatial distribution shows relatively high SNR for the pixels in the V-shape. This can be achieved by averaging over pixels with high SNR or it averaged over many pixels with low SNR. More can be seen from the distribution of the SNR as a function of emissivity in Fig. 4a), red markers represent all pixels while blue markers exclude cells in the magenta box in 4b). The convergence of the V-shape towards the camera pupil, where the
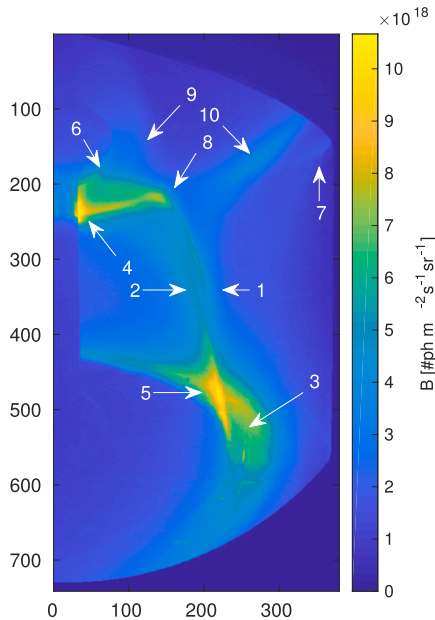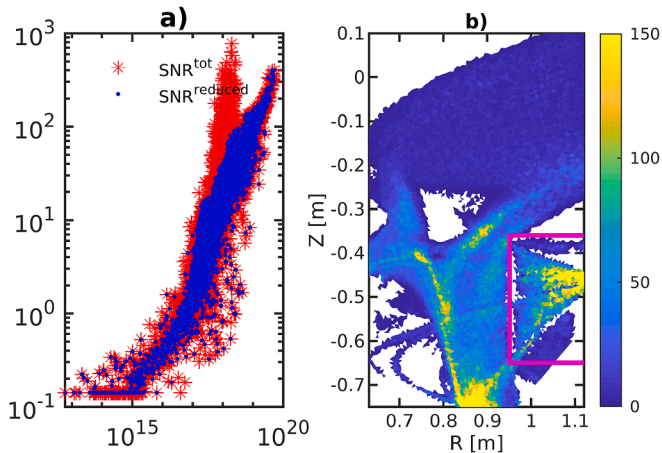

Fig. 2. Outer target common flux (1), private flux (2), outer target (3), inner target (4), overlap between the outer target and the private flux (5), inner and outer baffle interaction (6,7), emission near the X-point (8) and the upstream emission for inner and outer targets and far SOL(9,10). MANTIS image of $D_{5\to2}$ in TCV # 63974, $t = 1.315$ s, $< n_e > = 1.15 \cdot 10^{20}$ m^{-3}. For an image of illuminated vacuum vessel see [25].

Fig. 4. a) Distribution of SNR as a function of emissivity; red markers present all inversion cells; blue markers exclude cells in the magenta box. b) Signal to noise ratio for each inversion cell. TCV $\#63974$, $t = 1.315\,\text{s}$.

number of rays per cell is the highest, suggests that it is the algorithm's way of producing evenly distributed light in the image.

To further study the importance of the V-shaped artifact, the inversion was split between the magenta box and the remaining cells and each part was separately forward-modeled finding that the V-shape produces diffused background around the main plasma features. This, indicates that the V-shape's main role is to match the diffused background consisting mainly of unstructured light and that it should be ignored in the analysis. Nevertheless, the artifact extends to the outer target suggests that a portion of light could be still misplaced. This should be taken into account when estimating the total photon emission from the outer target together with the reflection from the target itself.

4. Emissivity profiles

Calibrated inversions together with their uncertainty provide data for established Balmer analysis techniques to infer the local emission due to excitation and recombination [2]. In this section, this method will be used to split $D_{3\to2}$ into its excitation and recombination parts using $D_{5\to2}/D_{3\to2}$ line ratio. The method requires 2 Balmer lines assuming that: the emission comes from a plasma slab with constant n_e and T_e, the emission model is valid for Deuterium and the that the contributions from molecular reactions are negligible [33,2]. The molecular reactions can have a significant contribution to the lower-n Balmer lines appearing as excitation emission which locally can invalidate the assumption of the model [15,34]. Assuming the following plasma parameters: T_e ranging from $0.2\,\text{eV}$ to $500\,\text{eV}$; n_e in the range $10^{19}\,\text{m}^{-3}$ to $10^{20}\,\text{m}^{-3}$ and the neutral fraction n_0/n_e between 10^{-3} and 10^{-1}, the $D_{3\to2}$ emission can be split between excitation and recombination parts using $D_{5\to2}/D_{3\to2}$ line ratio. The fraction of light due to recombination, $F^{rec}_{3\to2}$ as a function of various plasma parameters is presented in Fig. 5. To propagate the parameter ranges, for each value of the ratio, the minimum and maximum values were used as uncertainty bounds while the mean $F^{rec}_{3\to2}$ was used further. The figure shows that as the plasma shifts towards the recombination dominated emission, the absolute uncertainty in F^{rec} increases due to plasma density dependence. To understand where does the experiment fall within this model, one should look at the experimental ratios and the respective inferred $F^{rec}_{3\to2}$ in Fig. 6. The figure shows an increase of the ratio in the Private Flux Region (PFR), on the High Field Side (HFS) and above the outer target while a lower ratio is observed at the target. This lowering at the target could be caused by the molecular reactions contributing to the lower n balmer lines, this results in a lower F^{rec}. Thus, the potential molecular contributions will appear as excitation emission.
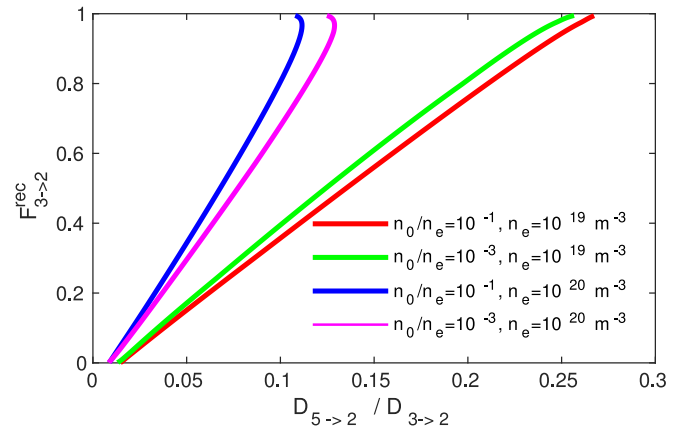

Fig. 5. Fraction of light due to recombination for T_e varied from 0.2 eV to 500 eV and fixed densities; $n_e = [10^{19}, 10^{20}]\,\text{m}^{-3}$ and neutral fractions; $n_0/n_e = [10^{-3}, 10^{-1}]$.
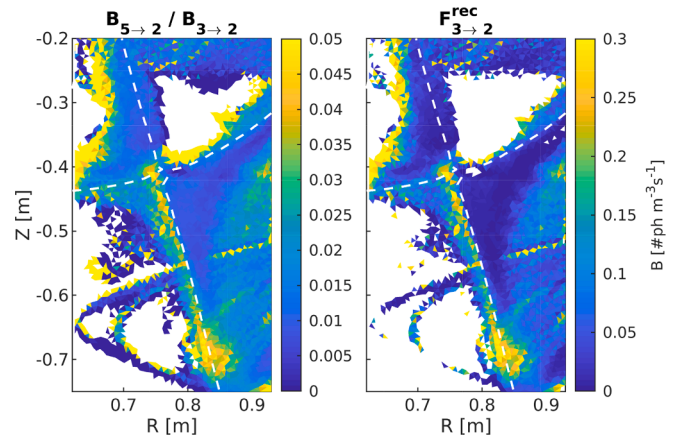

Fig. 6. Line ratio of $D_{5\to2}/D_{3\to2}$, and corresponding inferred F^{rec}. TCV $\#63974$, $t = 1.315\,\text{s}$. Dashed white contour marks the magnetic equilibrium separatrix.

The F^{rec} presented in the Fig. 6 was used to split the $D_{3\to2}$ emission into excitation and recombination fractions assuming that $F^{rec} + F^{exc} = 1$. The result of this split is presented in Fig. 7 showing the domination of excitation in the common flux from the X-point towards the targets. Following the field lines towards the outer target, the emission decreases and increases again at the outer target where the molecular reactions contributing to low n states are likely to occur [15,34]. The recombination part of the emission shows local maxima at both strike points and an additional one at the High Field Side (HFS) near the X-point.

This local maximum in recombination emission can be further investigated in the radial emission profiles in Fig. 8. The profiles were obtained by selecting cells within a region of interested marked in Fig. 7 for three time steps representing: attached conditions ($t = 0.8\,\text{s}, <n_e> = 6 \cdot 10^{19}\,\text{m}^{-3}$), peak outer target ion flux ($t = 1.28\,\text{s}, <n_e> = 11 \cdot 10^{19}\,\text{m}^{-3}$) and decreasing ion flux to the outer target ($t = 1.39\,\text{s}, <n_e> = 12 \cdot 10^{19}\,\text{m}^{-3}$). The cells were sorted based on their flux coordinate ρ_ψ value, to reduce the number of points, every 3 cells were averaged to produce a single radial point.

Looking at the outer target, at $t = 0.8\,\text{s}$, most of the emission is concentrated near the separatrix including both $\text{N\,II}$ at $399.5\,\text{nm}$ and $\text{C\,III}$ triplet at $465\,\text{nm}$. The $D_{3\to2}$ emission at the separatrix indicates excitation dominated plasma which is expected for attached conditions. This observation holds for both divertor legs.

As the time advances and the density increases, at $t = 1.28\,\text{s}$, the emission on both divertor legs remains peaked at the separatrix with a
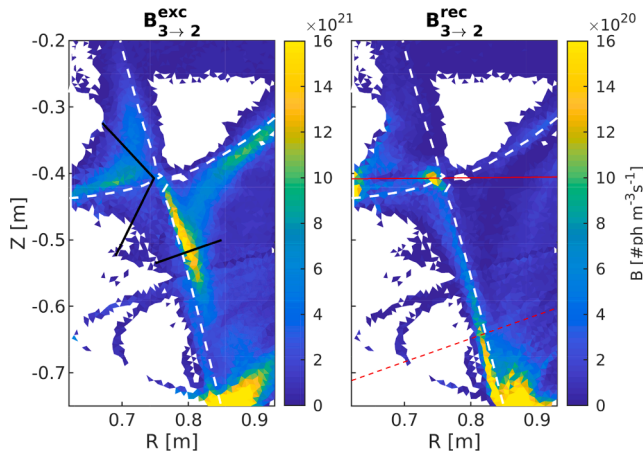
Fig. 7. $D_{3\to2}$ emission split between excitation and recombination parts using $D_{5\to2}/D_{3\to2}$, TCV #63974, $t = 1.315\,$s. Dashed white contour marks the magnetic equilibrium separatrix; black solid lines represent the regions of interest for radial profiles; red lines mark the DSS chords 31 and 5 for solid and dashed lines respectively.
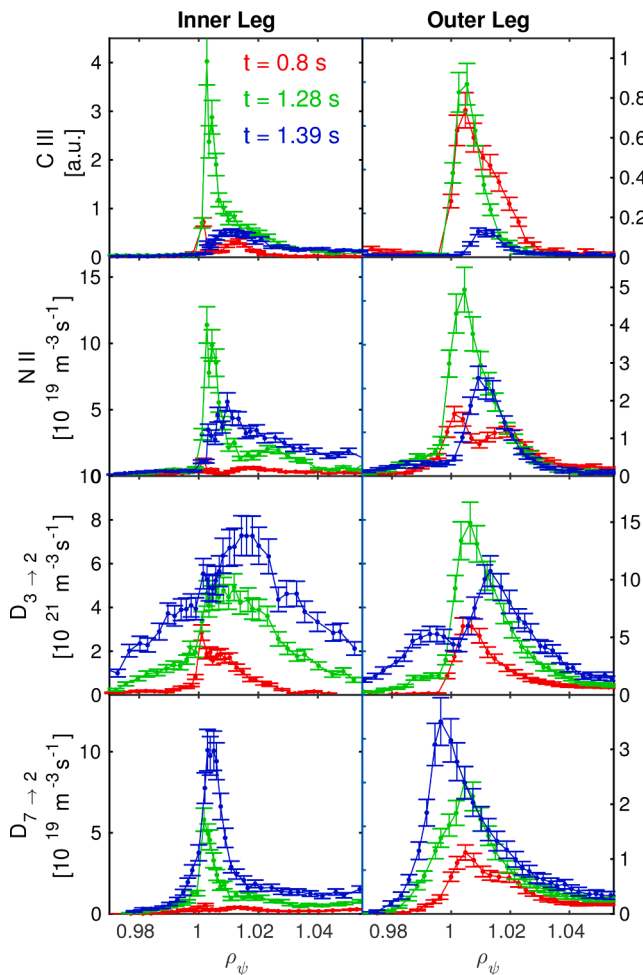

Fig. 8. Radial emission profiles for inner and outer divertor legs at regions of interest marked in Fig. 7 for attached, peak ion flux to the outer target and detached conditions. The impurity emission on the inner target increases disproportionately to the outer target prior to the rollover. In the final stage, at the outer target, the high and low n Balmer line maxima radially separate in opposite directions. TCV #63974.

considerable asymmetric increase of impurity emission on the inner divertor leg with respect to the outer. This results in a global maximum of impurity emission which is consistent with the global peak radiation obtained from bolometric data (not shown). The $D_{7\to2}$ emission on the inner leg forms a peaked profile near the separatrix, this can be indicative of recombination occurring in high density, potentially combined with a low temperature ($< 3\,$eV). Given that the emission coincides with the impurity emission of C III and N II, it indicates a peaked density profile on the inner divertor leg. To further investigate the origin of the $D_{7\to2}$ emission, the DSS was used to measure the plasma density with Stark broadening on $D_{7\to2}$ [34] resulting in $(11 \pm 2)\cdot10^{19}\,$m^{-3} for the highest chord and $(5 \pm 1)\cdot10^{19}\,$m^{-3} in the outer divertor leg at $t = 1.315\,$s. The chords are marked in Fig. 7. *This shows an accumulation of particles on the HFS near the X-point causing a local emission maximum for impurities and high n Balmer emission leading to a global maximum of plasma radiation.* Further in the density ramp, this HFS maximum can evolve into a HFS MARFE or rapidly disappear with an abrupt increase in the core density. The mechanisms behind this bifurcation are currently not identified.

Prior to the MARFE formation, the outer target ion flux rolls over causing further changes to the emission profiles. At $t = 1.39\,$s, the impurity emission decreases on both divertor legs indicating cooling below temperatures for efficient emission of C III and N II lines. The impurity emission maxima shift radially outward, a similar shift can be observed in $D_{3\to2}$ which appears to be consisting of two profiles: peaked and broad. The broader profile has an additional increase in the Private Flux Region (PFR). This spread of emission could be attributed to the Molecular Activated Recombination (MAR) processes at lower temperatures ($1-3\,$eV) [15]. The peaked part of $D_{3\to2}$ coincides with the impurity emission indicating processes occurring at higher temperature such as ionization. Contrary to the $D_{3\to2}$, the $D_{7\to2}$ emission maximum shifts inwards causing a radial separation between the maxima. Provided that the profile maxima of $D_{3\to2}$ and $D_{7\to2}$ represent excitation and recombination processes, this indicates a radial separation between density and temperature profiles. Such separation would result in a region of high density with low temperature promoting $D_{7\to2}$ emission and a region with low density and high temperature resulting in $D_{3\to2}$ emission.

5. Discussion and conclusions

The measurement technique for 2D emission profiles was presented together with uncertainty assessment. Resulting emissivities were used to split the $D_{3\to2}$ emission into excitation and recombination parts showing: a clear separation between emission in the private and common flux, a local emission maximum originating from accumulation of particles on the HFS near the X-point leading to a global maximum of plasma radiation. This HFS particle accumulation was inferred based on the line of sight integrated density measurement with Stark broadening and its location through the emission profile of $D_{7\to2}$. Those measurements are valid under the assumption of negligible impurity pollution in the $D_{7\to2}$ profile and T_e in the range for which the density measurement assumptions are valid. The separation into excitation and recombination also revealed that the emission at the outer target appears to be excitation dominated based on the $D_{5\to2}/D_{3\to2}$ ratio. This was attributed to other emission processes such as plasma-molecule interactions that locally break the assumption of the analysis.

The validity of those observations can be checked by following the DSS chord 31 intersecting the maximum in Fig. 7. The majority of its length passes through the excitation emission dominated plasma which can contribute to the total oxygen pollution in the DSS. The total amount of pollution was quantified in Fig. 1 b). For chords 29–31, the total line of sight integrated pollution is below 20% and it decreases during the experiment. Therefore, one can exclude that the $D_{7\to2}$ emission maximum at the HFS is found due to pollution alone.

The Fig. 8 reveals that the $D_{7 \to 2}$ emission can occur at the same location as the impurity emission. This indicates that the local T_e could be sufficient for excitation of impurities which may influence the density measurement due to temperature broadening. Later in the discharge, as the plasma cools, the impurity contribution and the electron temperature decreases improving both measurements while the observations remain valid. Therefore, the observation of the particle accumulation on the HFS cannot be explained by the density measurement assumptions nor the impurity pollution in the $D_{7 \to 2}$ filter.

Similar observations of a HFS High Density region was previously reported on ASDEX-U and JET [35,36]. However, there is a number of inconsistencies between the phenomena: in ASDEX-U it is found to occur in the far SOL instead of near the X-point. The TCV does not require detachment on the inner target to observe the phenomenon while it is found to be necessary on ASDEX-U [36].

The emission profiles presented in Fig. 8 show a considerable asymmetry between inner and outer targets together with a clear shift between high and low n Balmer lines for detached conditions. Previously at TCV, an assumption of separate temperatures for excitation and recombination was needed to explain the line integrated measurements [37]. Cited research suggested a presence of two emission weighted plasma regions which can now be spatially resolved. This separation can invalidate the assumption of emission originating from a uniform plasma slab, resulting in presence of recombination emission with inferred T_e^{rec} which is not representative for the ions arriving at the target. Provided that the radial separation scales to larger reactors, it would imply that the divertor detachment control cannot be based on the sole presence of recombination and T_e^{rec} below the divertor material requirements. Instead, the recombination rate together with the radial profile should be considered.

The experimentally observed features in the emission profiles are consistent with recent simulations employing the SOLPS-ITER code [14]. Referenced research presents formation of the X-point potential well resulting in $E \times B$ drift as a dominant radial particle transport in TCV. The simulations predict the drift direction and topology corresponding to the radial separation on the outer target as well as the HFS particle accumulation. To further investigate the phenomena, a detailed comparison between the experiment and the simulation would be required in future studies.

CRediT authorship contribution statement

A. Perek: Conceptualization, Software, Validation, Formal analysis, Investigation, Data curation, Writing - original draft, Writing - review & editing, Visualization. **B.L. Linehan:** Software, Validation, Formal analysis, Data curation. **M. Wensing:** Validation, Formal analysis, Conceptualization. **K. Verhaegh:** Validation, Formal analysis, Investigation, Conceptualization. **I.G.J. Classen:** Supervision, Project administration, Funding acquisition. **B.P. Duval:** Supervision, Project administration, Funding acquisition, Data curation. **O. Février:** Resources, Investigation. **H. Reimerdes:** Resources, Investigation. **C. Theiler:** Resources, Investigation. **T.A. Wijkamp:** Investigation. **M.R. de Baar:** Supervision, Project administration, Funding acquisition.

Declaration of Competing Interest

The authors declare that they have no known competing financial interests or personal relationships that could have appeared to influence the work reported in this paper.

Acknowledgments

References

[1] S.I. Krasheninnikov, A.S. Kukushkin, A.A. Pshenov, Divertor plasma detachment, Phys. Plasmas 23 (5). doi:10.1063/1.4948273.

[2] K. Verhaegh, B. Lipschultz, B.P. Duval, J.R. Harrison, H. Reimerdes, C. Theiler, B. Labit, R. Maurizio, C. Marini, F. Nespoli, U. Sheikh, C.K. Tsui, N. Vianello, W. A. Vijvers, Spectroscopic investigations of divertor detachment in TCV, Nucl. Mater. Energy 12 (2017) 1112–1117, https://doi.org/10.1016/j.nme.2017.01.004. URL:https://doi.org/10.1016/j.nme.2017.01.004, arXiv:1607.04539.

[3] H. Reimerdes, B.P. Duval, J.R. Harrison, B. Labit, B. Lipschultz, T. Lunt, C. Theiler, C.K. Tsui, K. Verhaegh, W.A. Vijvers, J.A. Boedo, G. Calabro, F. Crisanti, P. Innocente, R. Maurizio, V. Pericoli, U. Sheikh, M. Spolare, N. Vianello, TCV experiments towards the development of a plasma exhaust solution, Nuclear Fusion 57 (12). doi:10.1088/1741-4326/aa82c2.

[4] C. Theiler, B. Lipschultz, J. Harrison, B. Labit, H. Reimerdes, C. Tsui, W. Vijvers, J. A. Boedo, B. Duval, S. Elmore, P. Innocente, U. Kruezi, T. Lunt, R. Maurizio, F. Nespoli, U. Sheikh, A. Thornton, S. van Limpt, K. Verhaegh, N. Vianello, Results from recent detachment experiments in alternative divertor configurations on TCV, Nucl. Fusion 57 (7) (2017), 072008, https://doi.org/10.1088/1741-4326/aa5fb7.

[5] J.R. Harrison, C. Theiler, O. Février, H.D. Oliviera, R. Maurizio, K. Verhaegh, A. Perek, A. Karpushov, B. Lipschultz, B. Duval, J. Harrison, W. Vijvers, C. Theiler, B. Duval, X. Feng, S. Henderson, B. Labit, B.L. Linehan, A. Merle, H. Reimerdes, U. Sheikh, C.K. Tsui, W. Vijvers, C. Wuethrich, T. Team, E.M. Team, Progress Toward Divertor Detachment in TCV H-mode Discharges, submitted to Plasma Phys. Control. Fusion.

[6] O. Février, C. Theiler, J.R. Harrison, C.K. Tsui, K. Verhaegh, C. Wüthrich, J. A. Boedo, H. De Oliveira, B.P. Duval, B. Labit, B. Lipschultz, R. Maurizio, H. Reimerdes, Nitrogen-seeded divertor detachment in TCV L-mode plasmas, Plasma Phys. Controlled Fusion 62 (3) (2020), 035017, https://doi.org/10.1088/1361-6587/ab6b00.

[7] F. Nespoli, Scrape-off layer physics in limited plasmas in tcv, Ph.D. thesis, EPFL, Lausanne (2017). doi:10.5075/epfl-thesis-7475. URL:http://infoscience.epfl.ch/record/225542.

[8] R. Maurizio, B.P. Duval, J. Harrison, B. Labit, B. Lipschultz, H. Reimerdes, C. Theiler, K. Verhaegh, W. Vijvers, Divertor heat flux characterisation during detachment experiments in TCV, in: 44th EPS 44th Conference on Plasma Physics, 2017, p. 215001.

[9] O. Février, C. Theiler, H. De Oliveira, B. Labit, N. Fedorczak, A. Baillod, Analysis of wall-embedded Langmuir probe signals in different conditions on the Tokamak à Configuration Variable, Rev. Sci. Instruments 89 (5). doi:10.1063/1.5022459.

[10] C.K. Tsui, J.A. Boedo, J.R. Myra, B. Duval, B. Labit, C. Theiler, N. Vianello, W.A. Vijvers, H. Reimerdes, S. Coda, O. Février, J.R. Harrison, J. Horacek, B. Lipschultz, R. Maurizio, F. Nespoli, U. Sheikh, K. Verhaegh, N. Walkden, Filamentary velocity scaling validation in the TCV tokamak, Phys. Plasmas 25 (7). doi:10.1063/1.5038019.

[11] M. Wensing, B.P. Duval, O. Février, A. Fil, D. Galassi, E. Havlickova, A. Perek, H. Reimerdes, C. Theiler, K. Verhaegh, M. Wischmeier, SOLPS-ITER simulations of the TCV divertor upgrade, Plasma Phys. Controlled Fusion 61 (8). doi:10.1088/1361-6587/ab2b1f.

[12] N. Christen, C. Theiler, T.D. Rognlien, M.E. Rensink, H. Reimerdes, R. Maurizio, B. Labit, Exploring drift effects in TCV single-null plasmas with the UEDGE code, Plasma Phys. Controlled Fusion 59 (10). doi:10.1088/1361-6587/aa7c8e.

[13] A. Fil, B. Lipschultz, D. Moulton, B.D. Dudson, O. Février, O. Myatra, C. Theiler, K. Verhaegh, M. Wensing, Separating the roles of magnetic topology and neutral trapping in modifying the detachment threshold for TCV, Plasma Phys. Controlled Fusion 62 (3). doi:10.1088/1361-6587/ab69bb.

[14] M. Wensing, J. Loizu, H. Reimerdes, B.P. Duval, M. Wischmeier and the TCV team, X-point potential well formation in diverted tokamaks with unfavorable magnetic fild direction, Nuclear Fusion 60 (5) (2020) 054005. arXiv:arXiv:1011.1669v3, doi: 10.1017/CBO9781107415324.004.

[15] J.L. Terry, B. Lipschultz, A.Y. Pigarov, S.I. Krasheninnikov, B. LaBombard, D. Lumma, H. Ohkawa, D. Pappas, M. Umansky, Volume recombination and opacity in Alcator C-Mod divertor plasmas, Phys. Plasmas 5 (5) (1998) 1759–1766, https://doi.org/10.1063/1.872845.

[16] K. Verhaegh, B. Lipschultz, B.P. Duval, O. Février, A. Fil, C. Theiler, M. Wensing, C. Bowman, D.S. Gahle, J.R. Harrison, B. Labit, C. Marini, R. Maurizio, H. De Oliveira, H. Reimerdes, U. Sheikh, C.K. Tsui, N. Vianello, W.A. Vijvers, An improved understanding of the roles of atomic processes and power balance in divertor target ion current loss during detachment, Nuclear Fusion 59 (12). arXiv:1810.04969, doi:10.1088/1741-4326/ab4251.

[17] M.E. Fenstermacher, W.H. Meyer, R.D. Wood, D.G. Nilson, R. Ellis, N.H. Brooks, A tangentially viewing visible TV system for the DIII-D divertor, Rev. Sci. Instrum. 68 (1) (1997) 974–977, https://doi.org/10.1063/1.1147729.

[18] C.J. Boswell, J.L. Terry, B. Lipschultz, J. Stillerman, Applications of visible CCD cameras on the Alcator C-Mod tokamak, Rev. Sci. Instruments 72 (1 II) (2001) 935–939. doi:10.1063/1.1321010.

[19] J. Harhausen, A. Kallenbach, C. Fuchs, Interpretation of Dα) video diagnostics data as a contribution to plasma edge characterization, Plasma Phys. Controlled Fusion 53 (2). doi:10.1088/0741-3335/53/2/025002.

[20] A. Huber, S. Brezinsek, P. Mertens, B. Schweer, G. Sergienko, A. Terra, G. Arnoux, N. Balshaw, M. Clever, T. Edlingdon, S. Egner, J. Farthing, M. Hartl, L. Horton, D. Kampf, J. Klammer, H.T. Lambertz, G.F. Matthews, C. Morlock, A. Murari, M.

Reindl, V. Riccardo, U. Samm, S. Sanders, M. Stamp, J. Williams, K.D. Zastrow, C. Zauner, Development of a mirror-based endoscope for divertor spectroscopy on JET with the new ITER-like wall (invited), Rev. Sci. Instruments 83 (10). doi: 10.1063/1.4731759.

[21] M. Odstrčil, J. Mlynář, V. Weinzettl, P. Háček, T. Odstrčil, G. Verdoolaege, M. Berta, T. Szabolics, A. Bencze, Plasma tomographic reconstruction from tangentially viewing camera with background subtraction, Rev. Sci. Instruments 85 (1). doi:10.1063/1.4862652.

[22] W.A. Vijvers, G.P. Canal, B. Labit, H. Reimerdes, B. Tal, S. Coda, G.C. De Temmerman, B.P. Duval, T.W. Morgan, J.J. Zielinski, Power exhaust in the snowflake divertor for L- and H-mode TCV tokamak plasmas, Nuclear Fusion 54 (2). doi:10.1088/0029-5515/54/2/023009.

[23] J. Harrison, W. Vijvers, C. Theiler, B. Duval, S. Elmore, B. Labit, B. Lipschultz, S. van Limpt, S. Lisgo, C. Tsui, H. Reimerdes, U. Sheikh, K. Verhaegh, M. Wischmeier, U. Sheikh, Detachment evolution on the TCV tokamak, Nuclear Mater. Energy 12 (2016) 1071–1076, https://doi.org/10.1016/j.nme.2016.10.020.

[24] B.L. Linehan, R.T. Mumgaard, M. Wensing, K. Verhaegh, Y. Andrebe, J.R. Harrison, B.P. Duval, C. Theiler, The multi-spectral imaging diagnostic, Rev. Sci. Instrum. 89 (103503).

[25] A. Perek, W.A.J. Vijvers, Y. Andrebe, I.G.J. Classen, B.P. Duval, C. Galperti, J.R. Harrison, B.L. Linehan, T. Ravensbergen, K. Verhaegh, M.R. de Baar, Mantis: A real-time quantitative multispectral imaging system for fusion plasmas, Review of Scientific Instruments 90 (12) (2019) 123514. arXiv:https://doi.org/10.1063/1.5115569, doi:10.1063/1.5115569. URL:https://doi.org/10.1063/1.5115569.

[26] W. Vijvers, R. Mumgaard, Y. Andrebe, I. Classen, B. Duval, Conceptual design and proof-of-principle testing of the real-time multispectral imaging system mantis, JINST 12 (C07006).

[27] M.R.T., Engineering upgrades to the motional stark effect diagnostic on alcator c-mod engineering upgrades to the motional stark effect diagnostic on alcator c-mod, Ph.D. thesis, Massachusetts Institute of Technology (2015).

[28] W.J. Smith, Optical Coatings, McGraw-Hill Education, New York, 2008. URL: https://www.accessengineeringlibrary.com/content/book/9780071476874/chapter/chapter11.

[29] S. Silburn, J. Harrison, M. Smithies, A. Wynn, T. Farley, J. Cavalier, Calcam, doi: 10.5281/zenodo.1478555.

[30] M. Carr, A. Meakins, M. Bernert, P. David, C. Giroud, J. Harrison, S. Henderson, B. Lipschultz, F. Reimold, Description of complex viewing geometries of fusion tomography diagnostics by ray-tracing, Rev. Sci. Instruments 89 (8). doi:10.1063/1.5031087. URL:https://doi.org/10.1063/1.5031087.

[31] M. Carr, A. Meakins, S.A. Silburn, J. Karhunen, M. Bernert, C. Bowman, A. Callarelli, P. Carvalho, C. Giroud, J.R. Harrison, S.S. Henderson, A. Huber, B. Lipschultz, T. Lunt, D. Moulton, F. Reimold, Physically principled reflection models applied to filtered camera imaging inversions in metal walled fusion machines, Rev. Sci. Instruments 90 (4). doi:10.1063/1.5092781. URL:https://doi.org/10.1063/1.5092781.

[32] J. Karhunen, M. Carr, J.R. Harrison, B. Lomanowski, I. Balboa, P. Carvalho, M. Groth, A. Huber, G.F. Matthews, A. Meakins, S. Silburn, Effect of reflections on 2D tomographic reconstructions of filtered cameras and on interpreting spectroscopic measurements in the JET ITER-like wall divertor, Rev. Sci. Instruments 90 (10). doi:10.1063/1.5118885. URL:https://doi.org/10.1063/1.5118885.

[33] M.O.H. Summers, Atomic data and analysis structure, Tech. Rep. JET-P9735 (2000).

[34] K. Verhaegh, Spectroscopic investigations of detachment on TCV, Ph.D. thesis, University of York (September 2018).

[35] S. Potzel, M. Wischmeier, M. Bernert, R. Dux, H.W. Müller, A. Scarabosio, A new experimental classification of divertor detachment in ASDEX Upgrade, Nuclear Fusion 54 (1). doi:10.1088/0029-5515/54/1/013001.

[36] S. Potzel, M. Wischmeier, M. Bernert, R. Dux, F. Reimold, A. Scarabosio, S. Brezinsek, M. Clever, A. Huber, A. Meigs, M. Stamp, Formation of the high density front in the inner far SOL at ASDEX Upgrade and JET, J. Nucl. Mater. 463 (2015) 541–545, https://doi.org/10.1016/j.jnucmat.2014.12.008. URL:https://doi.org/10.1016/j.jnucmat.2014.12.008.

[37] K. Verhaegh, B. Lipschultz, B.P. Duval, A. Fil, M. Wensing, C. Bowman, D.S. Gahle, Novel inferences of ionisation and recombination for particle/power balance during detached discharges using deuterium Balmer line spectroscopy, Plasma Phys. Controlled Fusion 61 (12). arXiv:1903.08157, doi:10.1088/1361-6587/ab4f1e.